An Improvement on Land Surface Temperature Determination by Producing Surface Emissivity Maps

M. Pahlevani[a], M.R. Mobasheri[b*]

[a] *MSc. student of Remote Sensing, K. N. Toosi University of Technology, Tehran, Iran*
[b] *Associate Prof., K.N. Toosi University of Technology, Tehran, Iran*

Abstract

Emissivity mapping of the Earth's surface is the prerequisite to thermal remote sensing. A precise determination of a surface's temperature is dependent upon the availability of precise emissivity data for that surface. The present study area is a part of sugarcane plantation fields in the west part of Khuzestan province. In this work, Temperature Emissivity Separation algorithm (TES) was applied to five different ASTER L1B images. It was found out that TES method overestimates temperature in all the five thermal bands, and underestimates the emissivities as compared to the laboratory values. The differences in the emissivity values (as compared to laboratory values) varied from 10% in band 10 to 3% in band 14. The main reasons for these discrepancies were a lack of proper calibration of the thermal bands, the possible presence of radiometric noises in the calculation of the emissivity Maximum Minimum Differences (MMD) as well as mixed pixels. To overcome these uncertainties in the TES algorithm, an Improved TES method (ITES) was introduced. In the ITES method, the surface exiting thermal fluxes were simulated. The emissivities of four different reference surfaces, along with air temperature measured at nearby weather stations (believed to represent LST of full vegetated pixels) and the band 14 temperature, were employed as inputs. The results show noticeable improvements in the predicted emissivity to around 1% for band 10 and less than 1% for bands 13 and 14 as compared to the corresponding laboratory values. The root mean square error (RMSE) of emissivities for full vegetation cover was less than 0.015 and less than 0.01 for partial vegetated cover, bare soil, and sea water surface. Finally, emissivity maps for one sample image, employing the five thermal bands, were produced. It is believed that these maps can be used in other satellite images as layers of emissivity values for the purpose of a proper estimation of surface temperatures.

Keywords: Remote sensing; ASTER; TES algorithm; Emissivity mapping

1. Introduction

Land surface emissivity is a key parameter for determination of Land Surface Temperature (LST) as well as in the environmental studies. Most natural surfaces are able to emit only part of their potential radiant energy (Caselles et al., 1997). Therefore, direct temperature measurements by infrared (IR) thermometers (on a remote sensing system) can only give the radiant (apparent) temperature, which is known as the brightness temperature. In order to obtain the true or kinetic temperature, the emissivity of the observed surface must be known with an acceptable level of accuracy.

Many fields of studies such as geology, hydrology, vegetation monitoring, energy balance (evapotranspiration), desertification processes, land degradation, climate change, and global circulation models rely on the LST values with different levels of precision (Van de Griend and Owe, 1993; Sobrino et al., 2001; Mobasheri et al., 2007; Mobasheri, 2006; Lyon, 1965; Kerr et al., 2004; Jiménez-Muñoz et al., 2006 and Gillespie et al., 1998). Among these applications, desertification (through monitoring

vegetation water stresses and evapotranspiration) and land degradation process monitoring in a region are the most challenging topics that deserve special attention. Due to the fact that the spectral behavior of bare soils and desert land surfaces in thermal portion of the electromagnetic spectrum, are not changing within short lapses of time, any emissivity maps produced for these regions may persist for long and could be used for precise LST determination in these regions.

In order to retrieve accurate LST values from remote sensing or satellite data, the image must be accurately corrected for the emissivity of the surface of interest, as well as for atmospheric effects. Since 1970s, several techniques to perform these corrections have been published, with most of them applied to thermal data acquired at wavelengths between 8 and 14 μm. Different approaches have been used for retrieving LST and emissivity (Becker and Li, 1995; Dash et al., 2002; Kerr et al., 2004; Sobrino and Raissouni, 2000; Sobrino et al., 2001). Along with atmospheric and emissivity corrections, angular effects must also be corrected for, particularly for off-nadir views. The problem of angular effects on atmospheric parameters has been to a large extent solved, since radiative transfer codes like MODTRAN (Abreu and Anderson, 1996; Berk et al., 1999) allow the estimation of these parameters depending on the observation angle. However, the angular variation of land surface emissivity is not a well-known problem, especially for bare

surfaces of soil and rocks. In general, an uncertainty in the emissivity of about 0.01 leads to an error in the LST estimate of about 0.75 K for a fixed amount of radiant flux density at 300K (Mobasheri, 2006).

Emissivities are also important because they may be diagnostic of composition, especially for silicate minerals. Emissivity is thus important for studies of soil development and erosion and for estimating the amounts and changes in sparse vegetation cover, in addition to bedrock mapping and resource exploration (Gillespie et al., 1998). Direct measurements of emissivity of the ground surface are difficult, time consuming, and expensive. On the other hand, simultaneous determination of LST and emissivity is not possible even if the signal has been corrected for atmospheric effects, because measurements in *n* spectral bands of the thermal region leads to *n* equations that are always less than the *n+1* unknowns, i.e., *n* spectral band emissivity values plus one LST value. This difficulty can be addressed by using the functional relationship between vegetation index and radiometric surface temperatures. With vegetation indices such as the Normalized Difference Vegetation Index (NDVI), there is potential to relate this index to temperature at the NDVI pixel resolution, which is usually higher than the resolution of the thermal bands.

The governing thermal equation for the radiance reaching the sensor is of the form (Mobasheri, 2006):

$$L(x_n, y_m, \lambda) = \tau(x_n, y_m, \lambda) \begin{bmatrix} \varepsilon(x_n, y_m, \lambda) B_\lambda(T_{x_n, y_m}) + \\ \rho(x_n, y_m, \lambda) M(x_n, y_m, \lambda) \end{bmatrix} + S\uparrow(x_n, y_m, \lambda) \qquad (1)$$

where;

$$M(x_n, y_m, \lambda) = S\downarrow(x_n, y_m, \lambda) + \sum_{i=-\infty}^{+\infty} \sum_{j=-\infty}^{+\infty} R(x_{n+i}, y_{m+j}, \lambda)$$

In which x_n, y_m are the pixel position coordinates in the scene, $S\downarrow$ is the downwelling directional irradiance, $S\uparrow$ the upwelling directional radiance, L is the sensor received directional radiance, and R is the radiance emitted by the adjacent pixels, (all in W m^{-2} sr^{-1} μm^{-1}), ε is the spectral emissivity, ρ the spectral reflectance, T is the pixel kinetic temperature, and τ the atmospheric transmissivity. As can be seen in equation (1), all terms are pixel dependant and may vary from pixel to pixel. This renders a treatment of such equations very difficult.

Inversion of equation (1) for T and ε has been attempted using deterministic and nondeterministic approaches; the former approaches are applicable to areas for which one

or more of the unknowns is known (Labed and Stoll, 1991).

The task of temperature measurement for scenes such as oceans, snowfields and glaciers, and closed-canopy forests is deterministic (Labed and Stoll, 1991). However, deterministic solutions require that the atmospheric parameters in equation (1) be directly measured, but this is not always feasible.

Methods such as "split-window" algorithms rely on empirical regressions relating surface radiance measurements to surface temperatures (Mobasheri, 2006). Many attempts have focused on extending the "split-window" technique to land surfaces (Abrams and Hook, ASTER User Handbook). However, they all involve large errors due to the unknown surface emissivity differences. This introduces an even a greater

source of inaccuracy than the atmospheric effects (Tonooka et al., 2005). In general, land surface emissivities must be accurately measured if accurate kinetic temperatures are to be recovered.

As mentioned before, most channels measure data in the 8 to 14 μm region. The Advanced Spaceborne Thermal Emission and Reflection Radiometer (ASTER) was launched on the first of NASA's Earth Observing System polar-orbiting spacecrafts, EOS-1. This sensor consists of fourteen channels, five of which are devoted to the thermal-infrared (TIR) region of the spectrum from 8 to 14μm (Table 1) for the purpose of land-surface "kinetic" temperatures and emissivities retrieval, especially where none of these parameters are known as a priori. Because of their high spatial resolution (90 m), ASTER T and ε data can be verified through field experiments and to some extent by spectral libraries if pure pixels can be identified.

In order to equalize the number of unknowns and measurements so that the set of Planck equations for the measured thermal radiances can be inverted to temperature and emissivities, a Temperature and Emissivity Separation (TES) algorithm is developed. This algorithm relies on an empirical relationship between spectral contrast and minimum emissivity determined from laboratory and field emissivity spectra. It is designed to produce the surface temperature in one band and emissivity in 5 bands.

Table 1: Characteristics of the ASTER Thermal Channels

Channel no.	Bandpass (m) (μm)
10	8.125-8.475
11	8.475-8.825
12	8.925-9.275
13	10.25-10.95
14	10.95-11.65

Surface temperatures are independent of wavelength and can be retrieved using even one single band radiance data, provided that the emissivity of the observed surface in that band is known. Except for land cover types such as water, vegetation, and snow or ice, however, the emissivity of the land surfaces are not known a priori, and must be determined to an acceptable degree of accuracy.

In the TES algorithm, the additional data comes from a regression between minimum emissivity and their spectral contrast with laboratory spectra. For this, at least three to four spectral bands are required to measure the contrast in the images. Therefore, it is necessary to have multispectral measurements to determine land surface temperatures. Gillespie et al. (1998) claimed that the ASTER's estimated

temperature accuracy at 300K is 1K, and 3K at 240K. However, the ASTER instrument team compensate all measurements for the atmospheric transmissivity and path radiance both of which are determined independently (Sobrino et al., 2005), and report values for downwelling sky irradiance. So it might be possible to calculate accurate values of T and ε.

In regions where the spectral contrast is low, such as vegetated areas, the emissivity can be retrieved through the NDVI index (Jiménez-Muñoz et al., 2006). This index can be calculated using channels 2 (red) and 3 (near IR) of ASTER, which are not within the thermal region of the spectrum. In this work, the capability of the TES algorithm to estimate surface emissivity is assessed using emissivity values calculated by NDVI as well as through library values.

2. Study Area

The study area is a part of the Amirkabir and Dea`bal-Khazaie sugarcane sites located in the north-west of Persian Gulf some 25 kilometers south of Ahvaz in Khuzestan province, Iran. The field is located in UTM Zone 38, between 30º50'N and 31º30'N latitude and 47º35'E and 48º30'E longitude (Fig. 1). The selection of this area was based on the availability of the field data required in this research as well as the existence of bare soil, vegetated cover and water surfaces in the very same scene. Of course once the methodology approved, the method can be applied to the desert regions as well.

3. Data Collection and Image Processing

The required standard Level 1-B Terra/ASTER images for the period 2004 to 2005, that covers different sugarcane growing seasons, were supplied. To ensure the quality of the satellite images, analysis of the weather conditions was carried out. Subsets of the satellite images for different times were produced. The images were corrected for atmospheric effects using the ATCOR-2 program. Input data for this program were the altitude above sea level, pixel size, date and time of image acquisition, calibration file, weather parameters such as humidity and visibility, sun azimuth, latitude, and longitude. In addition, geometrical correction was done by rotating the image by an angle given in the image's header [Aster User Handbook Version 2]. Maps at 1:25000 scale were used in the image geo-referencing control process. Some 20 frames of ASTER images were investigated, 5

frames suitable for the study region being selected. The acquisition dates of these images
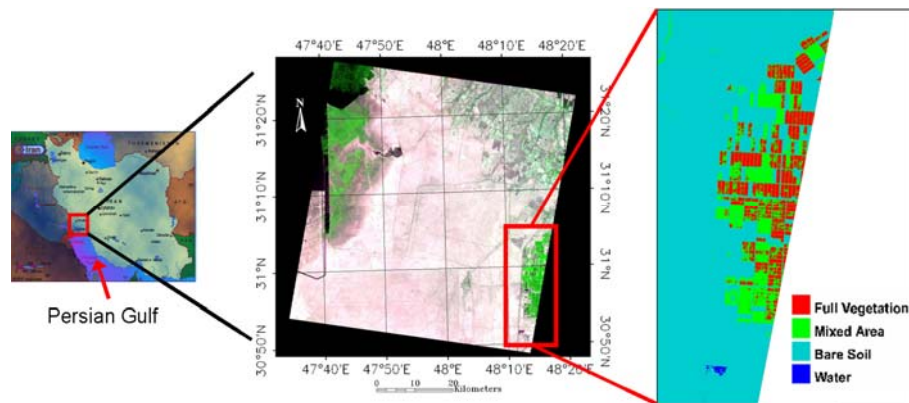
are shown in Table 2.

Fig. 1. Location of the study area in a sample image

Table 2. Some characteristics of the images used in this study

Image No.	Acquisition Date
1	Jun 9, 04
2	Jul 27, 04
3	Aug 5, 04
4	Sep 6, 04
5	Sep 9, 05

The availability of simultaneous field data and satellite images, along with the weather parameters collected from synoptic stations as well as the presence of vast homogeneous vegetated areas, made the study region suitable for the research.

4. Methodology

Following corrections and preprocessing stages, several reference vegetation covers were selected by imposing threshold values on the NDVI. The emissivities of these reference surfaces were evaluated by applying TES algorithm. These values were compared with those calculated using the NDVI method and those obtained from laboratory. Then the radiance flux densities were simulated and compared with those received through the sensors (after being corrected for atmospheric effects) and a linear regression between the two in each band were fit. Using these corrected radiance values, the TES algorithm was run again, where the resulting emissivities showed better agreement with those from the NDVI method and these from the spectral libraries.

One of the main problems in the assessment of remote sensing data compared to field data is the difference in the spatial scale of the two measurements. While field radiometric measurements have a representative scale of 1

m^2, the pixel area of ASTER is of the order of 8100 m^2. Comparisons between these two measurements are valid only when the test area (from the temperature and emissivity point of view) is homogeneous. Water surfaces, bare soils, dry lagoons, and dense vegetation canopies are example samples of these test areas, and can be used for testing the satellite thermal data (Tonooka et al., 2005). However, the variation of the emissivity of green vegetation in different parts of the thermal spectral region is minimal (Salisbury et al., 1988).

Many studies regarding water masses and sugarcane canopies have been conducted (Tonooka et al., 2005; Mobasheri, 2008; Mobasheri et al., 2007; Alesheikh et al., 2007).

The present study introduces an Improvement to TES algorithm (ITES) which is functional under any conditions. The presently used methods of emissivity estimation are initially critically reviewed. These are the TES algorithm and the NDVI method.

4.1. Temperature and Emissivity Separation Algorithm

The TES (Temperature and Emissivity Separation) is a method for the estimation of land surface emissivity ε_i and temperature T using ASTER land-emitted thermal radiation and down-welling atmospheric irradiances (Gillespie et al., 1998). The method is based on the radiative transfer equation applied to the thermal radiance L_i emanating from the surface (Jiménez-Muñoz et al., 2006):

$$L_i = \varepsilon_i B_i(T_s) + \pi^{-1}(1-\varepsilon_i)L_i^{atm\downarrow} \qquad (2)$$

where B_i is the Plank function for radiation flux density emanating from a Lambertian surface

with temperature T_s toward the sensor in a unit solid angle, $\pi^{-1}(1-\varepsilon_i)$. $L_i^{atm\downarrow}$ is the reflected downward sky thermal radiance from the surface in a unit solid angle toward the satellite sensor. What we receive at the sensor in channel i (L_{sen}^i) would then be:

$$L_{sen}^{i} = \tau_i L_i + L_i^{atm\uparrow} \qquad (3)$$

where τ_i is the band atmospheric transmittance and $L_i^{atm\downarrow}$ the atmospheric path radiance towards the sensor.

Using a proper atmospheric correction such as ATCOR2 or ISAC along with the atmospheric local parameters, one can extract L_i from equation (3) for each of the ASTER thermal channels. To solve Eq. (2) using data from five ASTER channels, one faces at least 6 unknowns: five radiation fluxes in five spectral bands and one surface temperature T_s. Thus, it is necessary to introduce one independent measurement. ASTER uses a semi-empirical relation between the minimum emissivity and spectral contrast (Maximum–Minimum Difference, MMD) determined from laboratory spectra.

Assuming L_i and $L_i^{atm\downarrow}$ as the input data and introducing an initial value for the emissivity in each band, five different values for the land surface temperature will be obtained, where the maximum value will be selected as T_s. This value can be introduced again in Eq. (2) to obtain the emissivity values for the ASTER thermal bands. This procedure can be repeated iteratively until convergence between these values occurs. This iterative procedure is called the NEM (Normalized Emissivity Method). In fact, equation (2) calculates 5 temperatures that are expected to be the same, but in practice, some differences do exist. These differences must be smaller than the noise equivalent temperature (NEΔT), which is about ± 0.3 K for the ASTER sensor (Abrams and Hook, ASTER User Handbook).

However, the accuracy of this method is limited. In order to obtain more accurate emissivity values, two other modules were deployed. These are the RATIO and the MMD (Maximum–Minimum Difference) modules. In the RATIO module, the ratio of NEM emissivity to the average value (β_i) was calculated, and in the MMD module the final values for the emissivity were obtained using the following expression:

$$\varepsilon_j = \beta_j \left(\frac{\varepsilon_{min}}{min(\beta_j)} \right) \qquad (4)$$

where ε_{min} is the minimum emissivity that can be obtained from the following empirical relationship (Gillespie et al., 1998):

$$\varepsilon_{min} = 0.994 - 0.687 \times MMD^{0.737} \qquad (5)$$

where MMD is the spectral contrast calculated as:

$$MMD = max(\beta_j) - min(\beta_j) \cdot \qquad (6)$$

The TES algorithm is capable of recovering surface emissivities within about 0.015 and surface temperatures within about 1.5K (Gillespie et al., 1998). However, for surfaces with low spectral contrast (MMD<0.03), the results are not convincing. In these cases, the TES algorithm sets ε_{min} to 0.983, a value that is appropriate for water and vegetation canopies (Gillespie et al., 1998).

Although this threshold value for MMD improves computations of temperatures for targets with low MMD, the case is problematic for targets with emissivities close to the threshold value (0.03). This can occur at transitions ranging from vegetation to soil.

4.2. NDVI Method of Land Surface Emissivity Determination

Because of uncertainties involved with the TES algorithm, the surface emissivity was calculated by another method independent of the thermal data. For this, different approaches based on NDVI values have been introduced most of which are based on the following simplified equation for homogeneous and flat surfaces (Sobrino and Raissouni, 2000; Lyon, 1965; Valor and Caselles 1996):

$$\varepsilon_i = \varepsilon_{vi} P_v + \varepsilon_{si}(1 - P_v) + C_i \qquad (7)$$

where ε_{vi} and ε_{si} are the band emissivity values for vegetation and for bare soil, respectively, and P_v the fractional vegetation cover. C_i is a term for empty spaces within the canopy and depends on the canopy internal reflectance, canopy structure and geometry. For a homogeneous field with a known soil composition, C_i can be set to zero (Sobrino et al., 2001) as is the case in this work. P_v can be obtained from NDVI values according to (Valor and Caselles 1996):

$$P_v = \left(\frac{NDVI - NDVI_s}{NDVI_v - NDVI_s} \right)^2 \qquad (8)$$

where $NDVI_v$ and $NDVI_s$ are the NDVI values of full vegetation cover (P_v=1) and bare soil (P_v=0), respectively, which can be obtained from the NDVI histogram. In those pixels with NDVI<$NDVI_s$, P_v will be set to zero, whereas for those pixels with NDVI>$NDVI_v$ the P_v will be set to 1.

The critical issue in Eq. (7) is the selection of the soil emissivities. The results of Eq. (8) are accurate enough to retrieve surface emissivities

from Eq. (7) (Abreu and Anderson, 1996). The NDVI index can be obtained using ASTER reflectance in bands 2 (RED) and 3 (NIR) through the following equation:

$$\text{NDVI} = \frac{\text{NIR} - \text{RED}}{\text{NIR} + \text{RED}}. \qquad (9)$$

The NDVI method data when compared with the field measured data shows a RMSE of less than 0.005 for full vegetated pixels and a RMSE of about 0.015 for bare soil (Tonooka et al., 2005; Van de Griend and Owe, 1993). Thus, emissivity values retrieved, using the NDVI method are comparable to the actual ones at an acceptable level of accuracy. Selection of soil emissivity in equation (7) is an important task which depends upon reconnaissance of the soil composition in the region of interest. The ASTER spectral library (http://speclib.jpl.nasa.gov) contains 52 soil classes. The extracted reflectance data for bands 10 to 14 (8.3-11.3μm) along with Kirshohf's law of $\varepsilon_j = 1 - \rho_j$ (ε_j and ρ_j are emissivity and reflectance in band j respectively) were employed for the emissivity calculations.

According to collected information from the region (Mobasheri, 2008), the soil in the study area stands in the Inceptisol class. The average value of the 7 different soils in this class was used in this research. Highly vegetated cover behaves like a blackbody, and a constant value of $\varepsilon_{v,j} = 0.99$ is applied for the emissivities in all ASTER thermal channels for full vegetated pixels in the study area (Mobasheri, 2006).

Based on the NDVI method, different surface covers, such as bare soil, sparsely vegetated areas, full vegetation cover, and water surfaces, can be differentiated (Valor and Caselles, 1996). The method of differentiation is the definition of some thresholds, i.e., NDVI<0.2 for soil, $0.2 \leq \text{NDVI} \leq 0.5$ for sparse vegetated cover, and NDVI>0.5 for full vegetated cover (Sobrino et al., 2005). Based on these, values of $\text{NDVI}_s = 0.2$ for soil and $\text{NDVI}_v = 0.5$ for vegetation are employed in equation (7). Then for pixels with NDVI < NDVI_s one has $P_v = 0$, and for those pixels with NDVI > NDVI_v, $P_v = 1$.

5. Results and Discussion

Due to the complexities involved in a direct assessment of the emissivities through satellite images (Carlson and Ripley, 1997), a comparison between the satellite data, and the data resulting from the NDVI method and those retrieved from spectral libraries was carried out. Four different land surface covers in the region were selected. These were full sugarcane cover,

partly vegetated (different proportions), bare soil, and deep water bodies in the Persian Gulf. In all selected ASTER images, 5 to 10 pixels (90 meters) were selected as sample pixels for the different types of land cover. Generally, these kinds of pixels do not exhibit sensitivity to the wavelength compared to the bare soil and to the partly vegetated surfaces. In addition, the sensitivity of full vegetated areas, emissivity to the viewing angle is low and can be ignored (Sobrino et al., 2005).

Since the NDVI for full cover pixels is greater than 0.5, P_v in equation (7) is taken to be 1. The NDVI takes negative values for water surfaces. Figure (2) shows emissivity values extracted from five ASTER bands for full vegetated cover pixels using TES algorithm and the NDVI methods along with the emissivities of three other vegetation cover types (coniferous, grass and deciduous) extracted from the ASTER spectral library (http://speclib.jpl.nasa.gov) intended for a comparison. Since the emissivity curves from the NDVI method were all of the same nature, only one of them is shown.
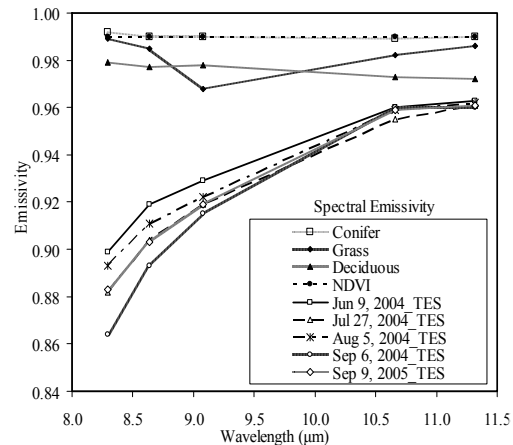

Fig. 2. Spectral emissivity calculated from the TES algorithm for five different dates and the NDVI method along with the emissivity curves for three other vegetation cover types

Figure (2) shows that the emissivity values calculated through NDVI method have a more or less uniform value of 0.99, and its standard deviation for the selected pixels was about zero, while the standard deviation using TES method was around 0.02. Moreover, the difference between the TES and NDVI methods was as high as about 11% in band 10, and as low as 3% in bands 13 and 14. This could be due to the relation between ε_{min} and MMD (equation 6), where the appearance of an MMD greater than

0.03 in this region causes the calculation of smaller emissivities than expected. The large difference between the emissivities in bands 10 to 12 for different dates could be due to the atmospheric effects.

As mentioned before, the TES algorithm is sensitive to spectral contrast while the range of emissivity values and temperature depends on MMD, so incomplete correction of atmospheric effects, especially downward scattered radiation, could effectively reduce the accuracy of the calculated emissivity values (Dash et al., 2002). On the other hand, bands 13 and 14 in the 10 to 12 m region can produce better results as compared to the other 3 thermal bands. This could be due to the reduction of atmospheric absorption in these spectral bands.

Figure 3 shows the emissivity values for the bare soil pixels produced through TES algorithm, NDVI method, and the ASTER spectral library. The region is a furrow field with an Inceptisol class of soil. The emissivity values calculated using the NDVI method reasonably match those extracted from the spectral library. This is not surprising because when we use equations (8) to calculate P_v, P_v would be zero because $NDVI<NDVI_s$ for all pixels, and consequently equation (7) gives the library values for the pixel emissivity. The reduction in the emissivity values in band 12 is due to the considerable fluctuation in the spectral emissivity of the Inceptisol class (Figure 3).
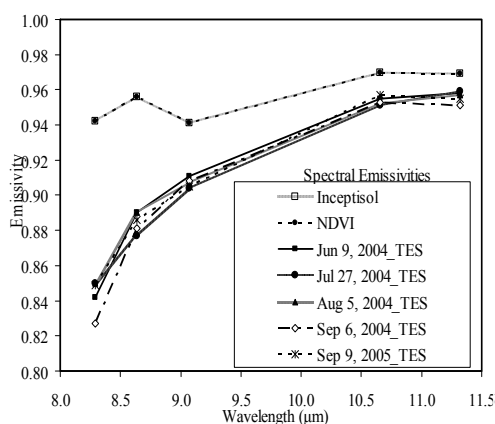

Fig. 3. Soil spectral emissivities calculated using different methods for five different ASTER images

The spectral emissivities calculated from the TES algorithm are more or less the same but smaller than those calculated from NDVI method and those extracted from spectral library curves. The difference is greater for shorter wavelengths i.e. about 10% for band 10, and 1% for bands 13 and 14. This could be due to the relationship between ε_{min} and MMD. However the standard deviation for the TES algorithm was on the order of 0.01.

For the mixed region of soil and vegetation, where the fraction of vegetation P_v is less than unity, the emissivity is expected to have values somewhere between soil and vegetation emissivities. The calculated emissivity using the TES algorithm for a P_v value of 0.5 for different ASTER images are shown in Figure (4). Emissivity calculated through NDVI method is also shown for comparison. Again, since the emissivity curves calculated through NDVI method for different dates were almost the same for each P_v value (with the standard deviation of less than 0.001) only one curve is shown. Although the emissivity curve calculated through TES is similar to those of bare soil and full vegetation, there are differences between these curves for different P_v values; the difference ranging from 9% in band 10 to 2% in bands 13 and 14. The standard deviation of the emissivities of the selected pixels (calculated through TES algorithm) was less than 0.01 for $P_v=0.5$. This could be due to inhomogeneity of the surface covers in this region. For the NDVI method, the standard deviation was found to be less than 0.001 for this case.

To analyze the emissivity of water surface calculated by TES algorithm, a region in the Persian Gulf was selected. To be able to compare the calculated emissivities with those obtained from spectral libraries, a region in the deep waters far from the shore was selected. Of course the NDVI method was not used in this case. Figure (5) shows the results of the TES algorithm for five ASTER images along with those collected from spectral libraries for frost water, foamy water, and sea water. In this case, as for full vegetation, the MMD values were higher than 0.03 because of low spectral contrast, and consequently the calculated emissivities were smaller than expected. In the sea water case, the difference between the TES emissivities and the spectral library values were higher in bands 10 to 12 (9%) while lower in bands 13 and 14 (3%).
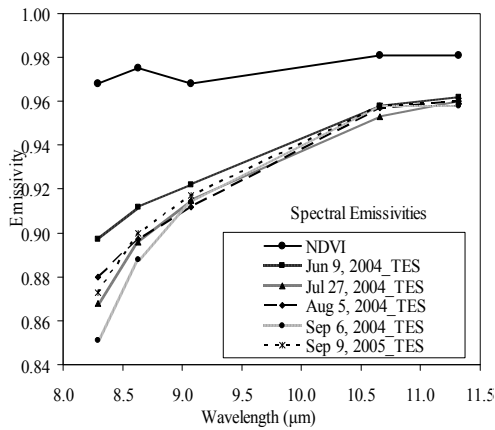
Fig. 4. Spectral emissivity calculated using different methods for $P_v = 0.5$ for 5 different ASTER images
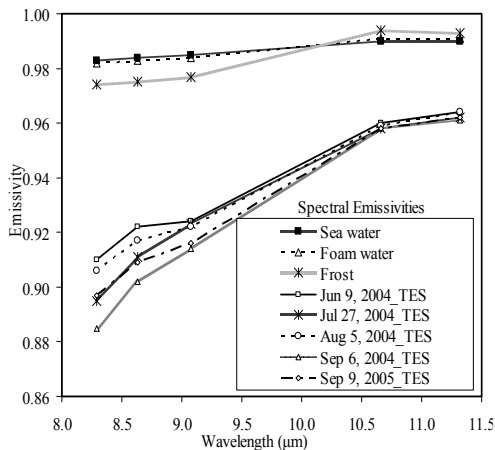

Fig. 5: Calculated sea water emissivities from the TES algorithm for 5 ASTER images along with the emissivity curves from laboratory values.

5.1. Improved TES Algorithm (ITES)

The results so far have demonstrated that the TES predicted emissivities do not have an acceptable accuracy and are always smaller than those calculated from the NDVI method and from the laboratory measured values. Generally speaking, this discrepancy comes from thermal band calibration, improper atmospheric corrections, and radiometric noise propagations. These effects are all wavelength dependent and cause inaccuracies in the MMD calculations, especially for surfaces with low spectral contrast. Analysis of each of these sources of error is difficult if not impossible.

According to the SEBAL algorithm (Carlson and Ripley, 1997), the temperature of a well watered full vegetation canopy can be considered to be the air temperature near the surface. As a result, the temperature in channel 14 for full vegetation can be compared with the air temperature measured at a nearby weather station. Of course, the horizontal gradient of the air temperature is considered to be smaller than the noise involved with the processed image. The temperatures collected from the weather stations at the satellite passing time are compared with those calculated from the TES algorithm (Table 3). It can be seen that the channel 14 temperature is always the closest value to the temperature measured at the weather stations, but always lower.

However, the band 14 emissivity values are in good agreement with values obtained using the NDVI method and those measured in the laboratory. Thus, the channel 14 TES measured temperature can be used as an initial guess of the true field temperature.

Table 3. TES calculated temperature minus 2 meters height weather temperature measured at nearby weather stations

Acquisition Date	Ch.10 (℃)	Ch.11(℃)	Ch.12 (℃)	Ch.13 (℃)	Ch.14 (℃)
Jun 9, 04	-4.74	-3.65	-2.95	-0.65	-0.40
Jul 27, 04	-7.68	-6.23	-5.44	-3.34	-2.90
Aug 5, 04	-4.68	-3.76	-3.19	-1.00	-0.62
Sep 6, 04	-6.27	-4.71	-3.55	-0.97	-0.62
Sep 9, 05	-5.63	-4.59	-3.70	-1.25	-1.15

The optical depth for July 27 is believed to have been high due to the presence of dust in the region and the resulting low visibility. At this stage, it is tried to develop a model to simulate the thermal spectral flux density received at the sensor using the temperature estimated from channel 14 and the following equation:

$$L_{j\_Simulated} = \varepsilon_j L_j^{BB}(T_{14}), \; j=10, 11, \ldots, 14. \quad (10)$$

In fact, equation (10) is an equivalent to the first part on the right hand side of equation (2),

where the effects of other radiance components such as path radiance and sky reflected radiation are included. Table (4) shows a list of emissivities obtained using the NDVI method and laboratory values used in this simulation. The simulated fluxes calculated from equation (10) were compared with those retrieved from ASTER sensor (after being corrected for atmospheric effects). A linear relationship between the simulated and measured radiances (L_j in equation 2) in each spectral band was found.

Table 4. Reference emissivities (ε_j) used for simulation

Land cover	Ch. 10	Ch. 11	Ch. 12	Ch. 13	Ch. 14
Full veg.	0.990	0.990	0.990	0.990	0.990
P_v~50%	0.968	0.975	0.968	0.981	0.981
Bare soil	0.942	0.956	0.941	0.970	0.969
Sea water	0.983	0.984	0.985	0.990	0.990

To develop a relationship between the simulated and measured radiances, three of the five ASTER images were employed. A linear fit to the simulated fluxes for different surface covers versus measured values in each band shows high correlations. The fitted equation was of the form:

$$L_j\_adj = A_j \times L_j + B_j. \tag{11}$$

The coefficients A and B and the R^2 for equation (11) are shown in Table (5).

Table 5. Coefficients used in equation (11)

Ch. No.	B_j	A_j	R^2
10	-0.265	1.133	0.993
11	0.147	1.071	0.997
12	1.431	0.931	0.994
13	0.948	0.941	0.997
14	0.813	0.946	0.998

Once again, the TES algorithm was applied to the ASTER images using simulated radiances. An initial value of 0.985 for emissivity, which is suitable for grey bodies, was introduced into the algorithm. According to Gillespie et al. (1998), a threshold value of 0.03 for calculated MMDs was used for the differentiation of pixels with low and high contrasts. If the apparent MMDs are larger than 0.03, ε_{min} can be calculated from equation (5), but for calculated MMDs less than 0.03, the estimated emissivities and temperature from the NEM will be selected as the final values and the processing stopped. This procedure results in higher emissivities for pixels with MMDs less than 0.03 and consequently produces less discontinuity in the spectral emissivity curves. Table (6) shows the MMDs calculated from the TES algorithm using simulated radiances for vegetation covers and sea water. It can be seen that, except for the case of full vegetation cover, the MMDs are less than the threshold value of 0.03.

Table 6. Averaged MMDs for vegetation cover and sea water extracted from the TES algorithm with simulated radiance applied to the ASTER images

Acquisition Date	Averaged MMDs For full veg. cover	Averaged MMDs For sea water
Jun 9, 04	0.015	0.004
Jul 27, 04	0.013	0.004
Aug 5, 04	0.011	0.006
Sep 6, 04	0.036	0.019
Sep 9, 05	0.018	0.011
Lab. values	0.003	0.007

The improved TES algorithm was then applied to the two remaining ASTER images of Jun 9, 2004 and Sep 6, 2004, that had not been used in the regression. The emissivities calculated through ITES, those calculated from the TES and NDVI methods, and laboratory obtained values are compared in Figure 6. As can be seen, the calculated emissivities using the ITES are in good agreement with those calculated through the NDVI method and the laboratory obtained values for all images.

In the case of full vegetation (Fig. 6), the maximum difference between the emissivities measured through the ITES and NDVI methods is about 3.4% in band 10. For other bands, the maximum difference is between 0.06 and 2%, which is more appropriate than what the TES algorithm produced before improvement. The case of fractional (50%) vegetation shows good agreement with the ITES and NDVI emissivities. Here, the highest discrepancy is 2.5% for band 10. The largest difference was about 10 to 13% for the TES algorithm where it shows acceptable improvements. For the other channels, the discrepancies reached 1.3% in the worst cases, which again were considerable improvements as compared to the TES results (4%). The difference between the ITES results and the NDVI (or laboratory) emissivity values for bare soil was about 3.8% for channel 10 and between 0 to 1.7% for the other channels. The difference for the TES algorithm stood between 4 and 11% respectively.

Note that the results so far have been compared with the NDVI calculated emissivities, where in the NDVI method we considered the best possible case i.e. the effects of empty spaces, shadows, while canopy internal reflections (C_j in equation 7) being ignored. In addition, the value of $\varepsilon_{s,j}$ in equation (7) is ideally selected from laboratory values for Inceptisol class soils, which is not the case in reality. Fig. (6) also shows the calculated emissivity of sea water from the ITES algorithm as well as from laboratory values. Again, the maximum difference between these two spectral curves is in band 10 and about 1.4%. This discrepancy could be due to the presence of surface suspended sediments such as kaolinite, orthoclase, chlorite, calcite, gypsum, muscovite, halite, anhydrite, apatite, biotite, quartz, and albite in the pixels (Mobasheri, 2008), so it is

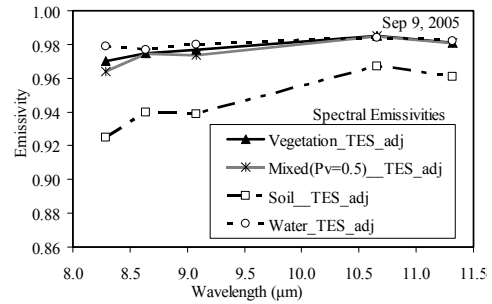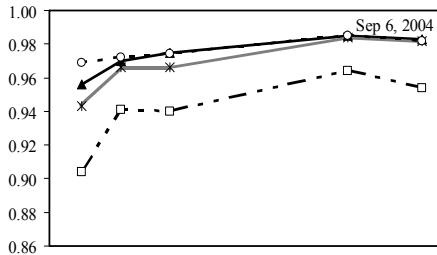expected that the emissivities of the pixels will be larger than that of sea water.
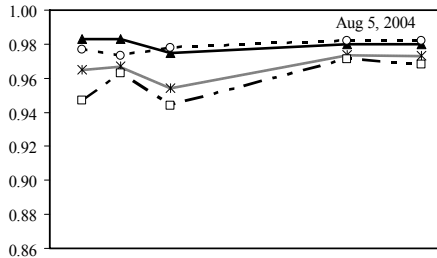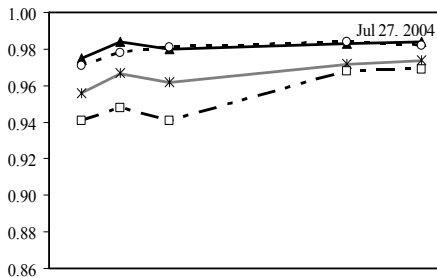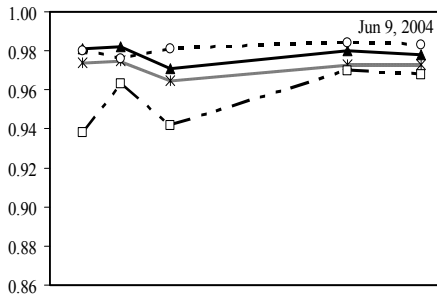

Fig. 6: Calculated emissivities using the ITES algorithm for full vegetation (sugarcane), mixed areas, bare soil, and sea water, for images from June 9, 2004, July 27, 2004, August 5, 2004, September 6, 2004 and September 9, 2005

5.2. Accuracy Assessment

To assess the accuracy of the ITES algorithm in surface emissivity prediction, the mean difference between ITES ($\varepsilon_i^{\text{ITES}}$) and NDVI (and/or laboratory) values ($\varepsilon_i^{\text{NDVI\&Lab}}$) were considered as biases, and the standard deviation of these biases for 5 thermal channels and RMSEs were calculated using the following equations:

$$\text{bias} = \frac{1}{5}\sum_{i=10}^{14}(\varepsilon_i^{\text{ITES}} - \varepsilon_i^{\text{NDVI\&Lab}}) \tag{12}$$

$$\text{RMSE} = \sqrt{\text{bias}^2 + \sigma^2}. \tag{13}$$

The calculated emissivity values for full vegetation covers have an RMSE less than 0.015. For partial vegetated covers, bare soil, and sea water, the calculated emissivity is less than 0.01. On the other hand, the maximum temperature among 5 thermal bands was selected as the surface temperature. This temperature was then compared with the air temperature measured at the nearby weather station. The RMSE for full vegetation surfaces was less than 1.5K.

5.3. Classification by emissivity values

In this work, four different classes of land covers were used as references. Using the emissivities of these references, one can calculate the temperatures of these references to an acceptable degree of accuracy.
Assuming a negligible horizontal temperature gradient for the region (a reasonable assumption in an ASTER scene), one can determine the temperature of the other pixels by interpolation between these reference temperatures. Using the produced layer of temperature and the ITES algorithm, one can produce a map of emissivity for the region. This is done for the ASTER

image of Aug 5, 2004. The output map of emissivity was sliced in steps of 0.01 and is
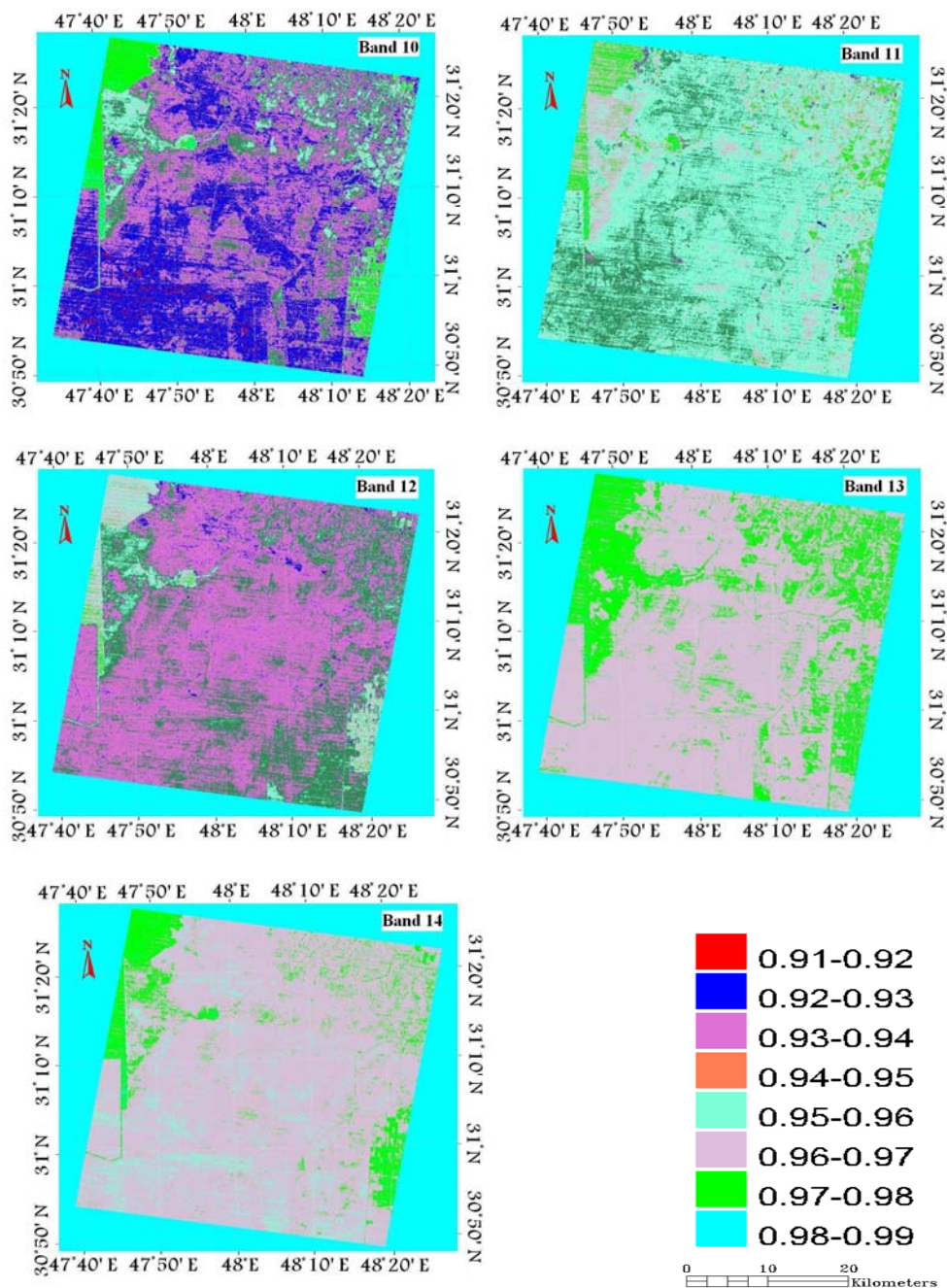
shown in Fig. (7) for all ASTER thermal bands.

Fig. 7. Emissivity maps in steps of 0.01 for five thermal bands in the Aug 5, 2004 ASTER image

6. Conclusion

The main goal of this study was to produce maps of emissivities using thermal bands of the high spatial resolution ASTER images. In this regard, the ability of the TES algorithm was

investigated using some reference surfaces with known emissivity values.

It was found that due to some sources of uncertainties, such as thermal band calibration, improper atmospheric corrections, and radiometric noise propagations, the TES

algorithm's outputs do not result in proper emissivity values and consequently produce incorrect temperature values. To overcome this difficulty, the flux densities received by the sensor were simulated using the highest TES predicted temperature (band 14) and the emissivities of reference surfaces. These simulated radiances were introduced in to the TES algorithm to obtain new values of temperature and emissivities.

This procedure continued for 2 to 3 iterations until stability in the values was achieved. This method is shown in Fig. (8) as a flowchart. Applying the produced emissivity maps to a limited region for 5 different dates, images of temperature in five bands were calculated and shown in Fig. (9). The results showed that this method is a success, and can modify the TES results for emissivity and temperature to an acceptable level of accuracy. The maps of

emissivities produced in this way can be used in other satellite images for upgrading their environmental parameter productions if precautions such as proper geo-referencing and spatial resampling are taken into consideration. To promote the applicability of this algorithm, we suggest the following: a) performing the absolute atmospheric correction using the proper atmospheric profile of the region, b) making field measurements of the emissivity of some reference surfaces that have negligible variation in time, c) using the recalibration method based on the image acquisition time and radiometric calibration coefficients (RCC) with versions 1.x and 2.x to minimize the calibration errors for ASTER thermal bands, and d) running the algorithm on additional images in different seasons of different years and from different geographical locations.
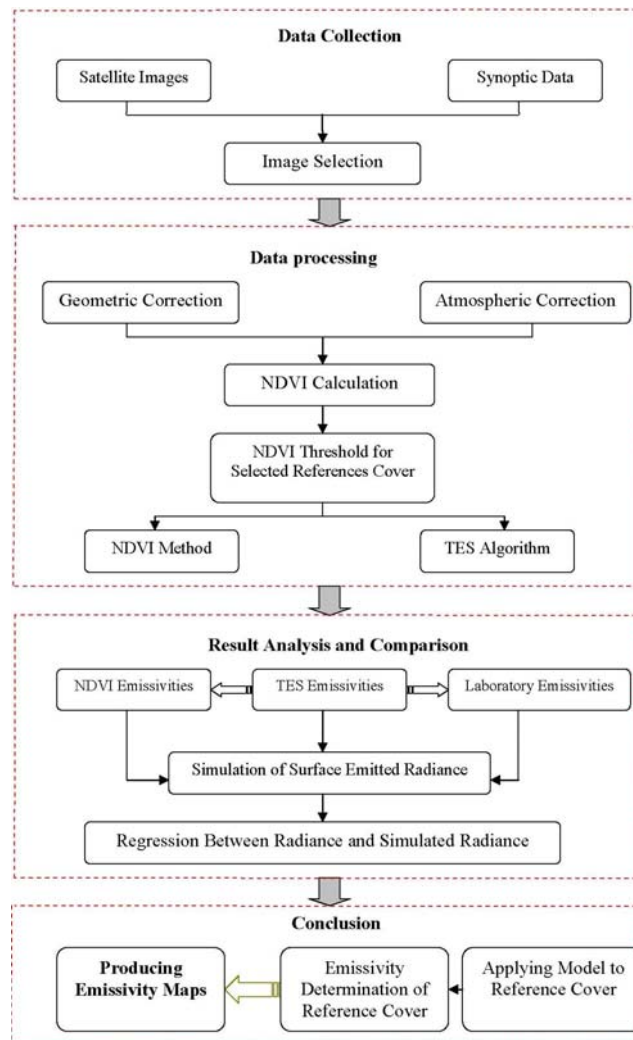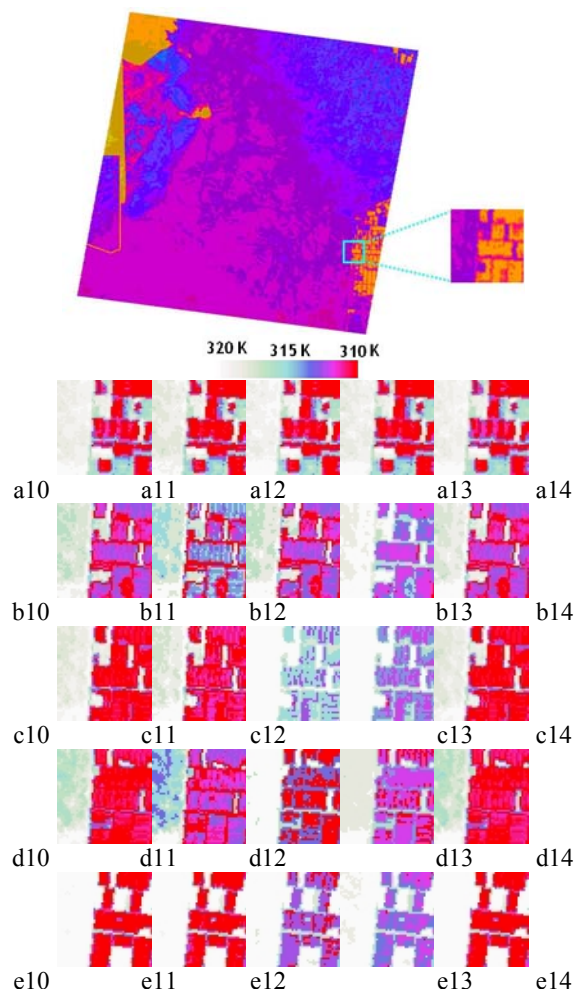

Fig. 8. Flowchart of the procedure of the research

Fig. 9. Images of LST for a sub region in ASTER bands 10, 11, 12, 13 and 14 after applying surface emissivity maps in 5 different dates a)-Jun9, 04; b)-Jul27, 04; c)-Aug5, 04; d)-Sep6, 04 and e)-Sep9, 05

References

Abrams, M. and S. Hook, ASTER User Handbook, Jet Propulsion Laboratory, Version 2, 4800 Oak Grove Dr., Pasadena, CA 91109.

Abreu, L.W. and G.P. Anderson, (Eds.), 1996. The MODTRAN 2/3 report and LOWTRAN 7 MODEL, Modtran report, contract F19628-91-C-0132: Philips Laboratory.

Alesheikh, Ali A., A. Ghorbanali, and N. Nouri, 2007. "Coastline Change Detection Using Remote Sensing" International Journal of Environmental Science and Technology, Vol. 4, No. 1, pp:61-66.

Becker, F. and Z. Li, 1995. Surface temperature and emissivity at various scales: Definition, measurement and related problem, Remote Sensing Reviews, 12: 225–253.

Berk, A., G.P. Anderson, P.K. Acharya, J.H. Chetwynd, L.S. Bernstein, E.P. Shettle, et al., 1999. MODTRAN 4 user's manual, Air Force Research Laboratory, Space Vehicles Directorate, Air Force Materiel Command, Hascom AFB, MA, pp. 95.

Carlson, T.N. and D.A. Ripley, 1997. On the relation between NDVI, fractional vegetation cover, and leaf area index, Remote Sensing of Environment, 62: 241−252.

Caselles, V., E. Valor, C. Coll and E. Rubio, 1997. Thermal band selection for the PRISM instrument: Part 1. Analysis of emissivity–temperature separation algorithms. Journal of Geophysical Research, 102: 11145– 11164.

Dash, P., F.M. Go¨ttsche, F.S. Olesen and H. Fischer, 2002. Land surface temperature and emissivity estimation from passive sensor data: theory and practice-current trends. International Journal of Remote Sensing, 23: 2563– 2594.

Gillespie, A., S. Rokugawa, T. Matsunaga, J.S. Cothern, S. Hook and A.B. Kahle, 1998. A temperature and emissivity separation algorithm for advanced spaceborne thermal emission and reflection radiometer (ASTER) images, IEEE Transactions on Geoscience and Remote Sensing, 36: 1113–1126.

Jiménez-Muñoz, J.C., J.A. Sobrino, A.Gillespie, D. Sabol and W.T. Gustafson, 2006. Improved land surface emissivity over agricultural areas using ASTER NDVI, Remote Sensing of Environment, 103: 474−487.

Kerr, Y.H., J.P. Lagouarde, F. Nerry and C. Ottle´, 2004. Land surface temperature retrieval techniques and applications: Case of AVHRR. In D.A. Quattrochi, and J.C. Luvall (Eds.), Thermal Remote Sensing in Land Surface Processes (pp. 33– 109). Florida, USA' CRC Press.

Labed, J. and P. Stoll, 1991. Angular variation of land surface spectral emissivity in the thermal infrared: Laboratory investigations on bare soils, International Journal of Remote Sensing, 12: 2299–2310.

Lyon, R.J.P., 1965. Analysis of rocks by spectral infrared emission (8 to 25 microns), Economic Geology, 60: 715−736.

Mobasheri, M.R., 2006. Fundamental of Physics in Remote Sensing and Satellite Technology (Farsi Ed.), Published by K.N.Toosi University of Technology, pp 318.

Mobasheri, M.R., 2008. Assessment of Suspended Sediment Concentration in Surface Waters, Using MODIS Images, American Journal of Applied Science, 5 : 798-804.

Mobasheri, M.R., J. Jokar, P. Ziaeian and M. Chahardoli, 2007. On the Methods of Sugarcane Water Stress Detection Using Terra/ASTER Images, American-Eurasian J. Agric. & Environ. Sci., 2: 619-627.

Salisbury, J.W., L.S. Walter and D.M. D'Aria, 1988.

Mid-infrared (2.5-13.5 μm) spectra of igneous rocks, U. S. Geological Survey Open-File Report 88-686, pp. 132.

Sobrino, J.A., J.C. Jiménez-Muñoz and W. Verhoef, 2005. Canopy directional emissivity: Comparison between models, Remote Sensing of Environment, 99: 304−314.

Sobrino, J.A., N. Raissouni and Z.L. Li, 2001. A comparative study of land surface emissivity retrieval from NOAA data, Remote Sensing of Environment, 75: 256–266.

Sobrino, J.A. and N. Raissouni, 2000. Toward remote sensing methods for land cover dynamic monitoring, Application to Morocco, International Journal of Remote Sensing, 21: 353−366.

Tonooka, H., F.D. Palluconi, S.J. Hook and T. Matsunaga, 2005. Vicarious calibration of ASTER thermal infrared channels, IEEE Transactions on Geoscience and Remote Sensing, 43: 2733−2746.

Valor, E. and V. Caselles, 1996. Mapping land surface emissivity from NDVI: Application to European, African and South American areas, Remote Sensing of Environment, 57: 167−184.

Van de Griend, A.A. and M. Owe, 1993. On the relationship between thermal emissivity and the normalized difference vegetation index for natural surfaces, International Journal of Remote Sensing, 14: 1119−1131.